The Astrophysical Journal, 578:503–514, 2002 October 10

STRINGENT X-RAY CONSTRAINTS ON MASS LOSS FROM PROXIMA CENTAURI

Bradford J. Wargelin and Jeremy J. Drake
Smithsonian Astrophysical Observatory, 60 Garden Street, Cambridge, MA 02138; bwargelin@cfa.harvard.edu, jdrake@cfa.harvard.edu
Received 2002 April 5; accepted 2002 June 12

ABSTRACT

We have analyzed data from two *Chandra* imaging observations of Proxima Centauri, searching for an X-ray halo arising from charge exchange between highly charged ions in its stellar wind and neutral gas in the surrounding interstellar medium. Based upon our model of Proxima Cen's charge exchange emission, the absence of any detectable charge exchange signal places a statistical 3 σ upper limit of $\sim 3 \times 10^{-13}\ M_\odot\ \mathrm{yr}^{-1}$ ($14\ \dot{M}_\odot$) on the mass-loss rate ($9\ \dot{M}_\odot$ for the 2 σ limit and $4\ \dot{M}_\odot$ for 1 σ), with a model uncertainty of roughly a factor of 3. This is orders of magnitude smaller than the upper limits that have been placed on late-type dwarf stars using radio observations, and it supports a recent mass-loss result for Proxima Cen based on Lyα absorption profiles. We have also studied the coronal spectrum, both in quiescence and during a prominent flare. Results are consistent with those obtained in previous X-ray observations, but a firm determination of coronal metal abundances remains elusive.

Subject headings: stars: coronae — stars: individual (Proxima Centauri) — stars: late-type — stars: mass loss — X-rays: stars

On-line material: color figures

1. INTRODUCTION

Proxima Centauri, a flaring M5.5 dwarf, is our nearest stellar neighbor and lies at a distance of 1.3009 ± 0.0005 pc (Benedict et al. 1999), roughly in the direction of the Galactic center ($l = 313\overset{\circ}{.}94$, $b = -1\overset{\circ}{.}93$). Proxima Cen's association with the binary system α Cen is controversial (Matthews & Gilmore 1993; Anosova, Orlov, & Pavlova 1994), as the $2\overset{\circ}{.}2$ separation between them corresponds to a large but poorly determined distance of at least a few thousand AU. However, the usual assumption is that Proxima Cen is a bound companion and shares the solar or greater photospheric metal abundances of α Cen AB. A rotation period of 83.5 ± 0.5 days, or perhaps half that, has been reported by Benedict et al. (1998), while Jay et al. (1996) have more tentatively suggested a 30 day period. Whichever period is correct, Proxima Cen is a slow rotator, consistent with its modest X-ray activity level, which is roughly one-quarter the saturation limit of $L_X/L_{bol} \sim 10^{-3}$ for active late-type stars (Agrawal, Rao, & Sreekantan 1986; Fleming et al. 1993).

In addition to having a surprisingly mysterious nature, Proxima Cen is intriguing as a representative of that most common class of fully fledged hydrogen-burning stars, the M dwarfs, and it is one of the few late M dwarfs close enough to allow characterization of its coronal emission, of which coronal metallicity is a particularly interesting parameter. The reviews of, e.g., Feldman & Laming (2000), Drake (2002), and White (1996) discuss evidence from *EUVE*, *ASCA*, and *BeppoSAX* spectra of active stars that indicates their coronae to be significantly metal-poor with respect to a solar composition, while Drake (2002) also presents evidence that less active stars can share the solar-like coronal "FIP effect," in which the coronal abundances of elements with low first ionization potentials (FIP $\lesssim$ 10 eV; e.g., Mg, Si, and Fe) are enhanced (relative to photospheric abundances) compared to the abundances of elements with high FIP ($\gtrsim$10 eV; e.g., O, Ne, and Ar). More recently, abundances derived from high-resolution *Chandra* and *XMM-Newton* spectra have indicated that in very active stars, the abundances of Ne, Ar, and possibly other high-FIP elements can be strongly enhanced relative to that of Fe (Drake et al. 2001; Brinkman et al. 2001; Phillips et al. 2001; Maggio et al. 2002).

Proxima Cen's stellar wind is also of great interest, since even a moderate M dwarf mass-loss rate would have important implications for the origin of cosmic-ray seed particles, as well as heavy-element dispersal, kinetic heating, and ionization throughout the interstellar medium (ISM). Mass loss is also of critical importance in models of angular momentum loss and other aspects of stellar evolution. With very few exceptions, however, existing measurements of stellar mass-loss rates do not extend below a few times $10^{-10}\ M_\odot\ \mathrm{yr}^{-1}$ (4 orders of magnitude higher than the solar rate of $\sim 2 \times 10^{-14}\ M_\odot\ \mathrm{yr}^{-1}$) and only apply to high-mass O and B stars, red giants, and supergiants.

Lim & White (1996) provide a good summary of theoretical and observational constraints on dwarf star mass-loss limits prior to 1997. A fairly recent theoretical effort is that of Badalyan & Livshits (1992), who predict that magnetically saturated M dwarf flare (dMe) stars can have winds with mass-loss rates exceeding $\sim 10^{-11}\ M_\odot\ \mathrm{yr}^{-1}$.

Perhaps the strongest observational evidence in favor of strong late-type dwarf winds comes from V471 Tau, an eclipsing binary consisting of a K2 V star and a white dwarf. Mullan et al. (1989) reported observing discrete absorption features in the UV continuum of the white dwarf and interpreted them as arising from a cool (10^4 K) wind with a mass-loss rate of $10^{-11}\ M_\odot\ \mathrm{yr}^{-1}$. Lim, White, & Cully (1996a), however, argue that the detection of nonthermal radio emission from this system implies that any wind from the K dwarf must be optically thin, which is probably inconsistent with the temperature and mass-loss rate inferred by Mullan et al. More recently, Bond et al. (2001) observed transient absorptions in the Si III 1206 Å line, which they ascribed to coronal mass ejections (CMEs). Based on the number of events and other viewing considerations, they estimate that the active K star "emits some 100–500 CMEs day^{-1}, as

compared to ~1–3 day^{-1} for the Sun. The K dwarf's mass-loss rate associated with CMEs is at least $(5–25) \times 10^{-14}$ $M_\odot$ yr^{-1}, but it may well be orders of magnitude higher if most of the silicon is in ionization states other than Si III."

Doyle & Mathioudakis (1991) and Mullan et al. (1992) have also reported marginal detections of millimeter radiation from several dMe stars, of which YZ CMi is the most significant example. Based on a 2.2 σ measurement at 1.1 mm and data in other wave bands from *IRAS* and the VLA,[1] Mullan et al. (1992) inferred that YZ CMi has an optically thick wind and loses mass at the rate of $\sim 5 \times 10^{-10}$ $M_\odot$ yr^{-1}. Houdebine, Foing, & Rodonò (1990) recorded optical spectra of another dMe star, AD Leo, and argued that based on the observation of a CME during a flare, the total flare-related mass loss was between 2.7×10^{-13} and 4.4×10^{-10} $M_\odot$ yr^{-1}. Lim & White (1996), however, argued that existing radio data on both stars indicate the existence of nonthermal coronal emission, which must arise near the stellar surface and then propagate through an optically *thin* wind to be detectable. Citing the detection of nonthermal emission from YZ CMi at 327 MHz (Kundu & Shevgaonkar 1988), they derive a more model-dependent upper limit of 5×10^{-14} $M_\odot$ yr^{-1} for a 300 km s^{-1} 10^4 K wind, or up to $\sim 10^{-12}$ $M_\odot$ yr^{-1} for a wind with temperature of $\sim 10^6$ K and velocity between 300 and 600 km s^{-1}. Van den Oord & Doyle (1997) similarly derived a limit of no more than $\sim 10^{-12}$ $M_\odot$ yr^{-1}, based on existing IR and radio observations of several dMe stars. For the specific case of Proxima Cen, based on its nondetection at 3.5 cm, Lim, White, & Slee (1996b) directly placed a 3 σ upper limit of $\sim 7 \times 10^{-12}$ $M_\odot$ yr^{-1} on its mass-loss rate, assuming a wind with $T \sim 10^4$ K and velocity ~300 km s^{-1} (or $\sim 10^{-11}$ $M_\odot$ yr^{-1} for $T \sim 10^6$ K).

In the past few years, several papers utilizing a different wind detection method have been published, based on the idea that interaction of an ionized stellar wind with neutral gas in the ISM, via proton-hydrogen charge exchange (CX), creates a "hydrogen wall" of warm neutral gas (Wood, Alexander, & Linksy 1996; Gayley et al. 1997; Izmodenov, Lallement, & Malama 1999). The signature of this gas is a slight excess of Lyα absorption, which has been detected, at least tentatively, in seven nearby stars (Wood et al. 2001 and references therein). In four of those systems, three of which are composed of late-type, main-sequence stars, the absorption is strong enough to have permitted mass-loss rate estimates: very roughly, $\dot{M} = 10\ \dot{M}_\odot$ for the active RS CVn type binary λ And (G8 IV–III+unknown) and 1 $\dot{M}_\odot$ for ϵ Ind (K5 V) (Müller, Zank, & Wood 2001); and $\dot{M} = 2\ \dot{M}_\odot$ for α Cen AB (G2 V+K0 V) and an upper limit of 0.2 $\dot{M}_\odot$ for Proxima Cen (Wood et al. 2001). Some of the assumptions used to derive those rates, however, particularly regarding the intrinsic Lyα profiles of the stars in question, are controversial, and the resulting uncertainties are not well understood. The D/H abundance ratios used in that work may also be less secure than was assumed (Vidal-Madjar & Ferlet 2002).

In an earlier paper (Wargelin & Drake 2001), we described a more direct method of investigating the winds of late-type dwarf stars, via the CX X-ray emission that results as highly charged ions in the wind, particularly oxygen, interact with neutral gas in the ambient ISM. The emission mechanism is essentially identical to that for comets, first explained by Cravens (1997), except that the neutral gas is primarily atomic hydrogen rather than water vapor. To briefly summarize, when a highly charged ion collides with neutral gas, an electron can be transferred from the neutral into an excited energy level of the wind ion, which then decays and emits an X ray. Two-electron CX occurs roughly 10% of the time in wind-comet interactions (Greenwood et al. 2000), but this process is unimportant in the H-dominated (single-electron) neutral gas considered here.

Soon after the first X-ray observations of comets, Cox (1998) pointed out that CX must occur throughout the heliosphere as the solar wind interacts with neutral gas in the ISM. Subsequent quantitative analyses (Cravens 2000; Cravens, Robertson, & Snowden 2001) determined that this mechanism accounts for a significant fraction of the observed soft X-ray background, in agreement with indications from *ROSAT* observations (Snowden et al. 1995) that roughly half of the $\frac{1}{4}$ keV background comes from a "local hot plasma." As discussed by Wargelin & Drake (2001), this same process must occur for any star with a highly ionized wind residing inside a partially neutral region of the ISM. By searching for the resulting distinctively profiled CX emission, stellar winds with mass-loss rates not much greater than the Sun's can now be detected around nearby stars with high-resolution, large-area X-ray observatories.

In this paper, we present results from *Chandra* observations of Proxima Cen, beginning with an overview of the data and a discussion of light curves in § 2, followed by spectral analysis of emission in quiescence and during a large flare in § 3. In § 4, we derive a sensitive upper limit to the stellar mass-loss rate, based on the observed level of CX X-ray emission, marking the first application of this wind detection method, and we conclude with a discussion of model uncertainties and prospects for reducing them.

2. THE OBSERVATIONS

Proxima Cen was observed twice by *Chandra* as a Guest Observer target (PI J. Linsky) between 2000 May 7 and 9. Both observations (observation IDs 49899 and 641) utilized the ACIS-S CCD array in imaging mode, for 29,856 and 19,036 s, respectively. The intention was to use ACIS-S with the High Energy Transmission Grating, but a hardware fault prevented insertion of the grating.

Standard *Chandra* X-Ray Center pipeline products were reprocessed to level 2 using the *Chandra* Interactive Analysis of Observations (CIAO) software version 2.1.3, taking advantage of recent gain map improvements for the central (S3) CCD released in CALDB version 2.8. Various energy filters were then applied to the data to increase the contrast of secondary X-ray sources against the background. About two dozen extraneous sources were removed from the S3 chip.

Unfortunately, because of the high counting rate of the source and the chosen CCD frame time (3.2 s), more than 95% of the events in the main peak were rendered useless because of pile-up and the associated phenomenon of grade migration, which lead to distorted spectra and nonlinear counting rates. To keep these effects at a negligible level, we had to exclude data from the central core of the source.

[1] The VLA (Very Large Array) is a facility of the National Radio Astronomy Observatory (NRAO). The NRAO is a facility of the National Science Foundation operated under cooperative agreement by Associated Universities, Inc.

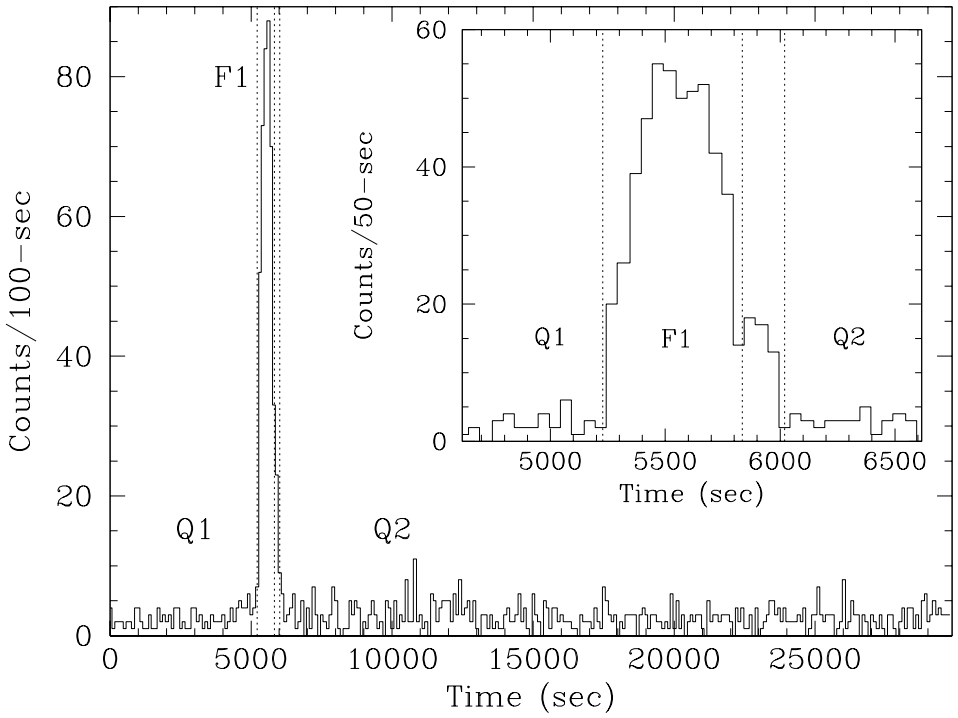

FIG. 1.—Light curve for observation ID 49899, using 100 s time bins (50 s for flare detail). Zero time corresponds to 2000 May 7, 22:56:24 UT. The spatial filter is an annulus of radii 4 and 30 pixels, plus the 2 pixel–wide readout streak (radii 4 and 80 pixels, with 3 pixel streak in flare detail). Background is 0.16 counts per 100 s time bin (0.40 per 50 s in flare detail). The Q1 and Q2 time ranges were included in the composite quiescent spectral analysis, and F1 was used for the flare analysis.

Because so few events were left, we included counts from the "readout streak" for use in spectral and light curve analysis. The streak is an artifact of the CCD readout process, with a net exposure time per frame equal to the number of CCD rows (1024) multiplied by the time required to shift the image by one row during readout (40 μs), or 0.041 s. The readout streak exposure efficiency when using a 3.2 s frame time is therefore $0.041/(3.2 + 0.041) = 1.26\%$, and pile-up is completely negligible.

Light curves for each observation ID (Figs. 1 and 2) were extracted from the source event files at energies up to 2 keV using annuli of radii 4 and 30 pixels (2″ and 15″), centered on the source, plus a 2 pixel–wide box to include the readout streak. Background rates were derived from the entire S3 chip, after we excluded extraneous sources, a 200 pixel radius circle around Proxima Cen, and a narrow strip around the edges of the chip. The background was statistically uniform across the chip and showed no significant temporal variability during either observation.

3. SPECTRAL ANALYSIS

3.1. *Data Extraction*

Based upon the light curves, we divided the observations into flare and quiescent time ranges for spatial and spectral analysis. The time ranges are marked as intervals F1, F2, and Q1–4 and are summarized in Table 1. The latter part of the flare (the 200 s between F1 and Q2) was not included in F1 in order to avoid "contamination" of the flare's point-spread function (PSF; see § 4.3). The 1000 s between Q3 and F2 were also not analyzed.

Readout streaks, typically containing one or two hundred counts, were used to estimate the true inner-core counting rate in the absence of pile-up, after we excluded a 50 pixel radius circle around the main peak and accounted for the minor effects of background and X-ray events in the PSF wings. Events from the background-subtracted outer core and wings were then added to give the total corrected rates. The preflare and postflare quiescent intervals of observation

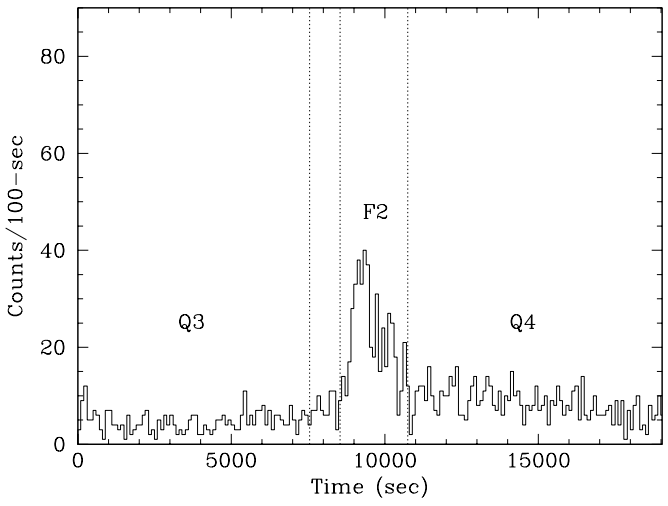

FIG. 2.—Light curve for observation ID 641, using the same spatial filter as for observation ID 49899. Zero time corresponds to 2000 May 9, 00:05:54 UT. Background is 0.16 counts per 100 s time bin. Q3 and Q4 were included in the quiescent spectral analysis.

TABLE 1
Spectral Data Extraction Parameters

Time Range	Annular Radii (pixels)	Streak Width (pixels)	Total Spectrum Counts	Estimated Background Counts	Corrected X-Ray Counts	Exposure Live Time (s)	Corrected Rate (counts s^{-1})
Q1+Q2	3, 30	2	983	47	19,330 ± 1560	28,688	0.67 ± 0.03
F1	4, 80	3	491	5	10,360 ± 950	592	17.5 ± 2.6
Q3	3, 35	3	475	18	7,690 ± 950	7,450	1.03 ± 0.13
F2	4, 60	3	566	11	13,420 ± 1130	2,172	6.18 ± 0.52
Q4	3, 40	3	914	23	16,800 ± 1300	8,186	2.05 ± 0.16

Note.—Spectra from time ranges Q1–Q4 were summed into a single quiescent spectrum for fitting. The spectrum of the large flare, F1, was also analyzed. "Corrected X-ray Counts" is the estimated total number of X-ray events (not including the readout streak) at energies below 2 keV if there had been no pile-up or grade migration effects. The live-time fraction is 0.987 for all time intervals.

ID 49899 (Q1 and Q2) have the same count rate, whereas the analogous intervals of observation ID 641 have higher rates that differ from each other by a factor of 2.

To maximize the number of counts available for spectral analysis, we adjusted the sizes of the annuli and readout streak boxes for each time interval, using as small an inner radius as possible on the annuli while keeping pile-up effects negligible. Inner radii were chosen by comparing the PSFs of low-rate and high-rate data with each other and with calibration models and by studying how spectral shapes and hardness ratios varied depending upon how much of the core was included in the extraction region. As shown in Table 1, we used an inner radius of 3 pixels for quiescent times and 4 pixels for the flares. Outer radii and readout streak box widths were chosen to include as many X-ray events as possible while keeping the relative background contribution low and were different for each time interval. Extracted spectra for each of the time ranges are shown in Figure 3. Data from Q1 and Q2 were combined, since their rates and spectra were the same.

Spectral analysis was performed with the CIAO SHERPA "fitting engine" (Freeman, Doe, & Siemiginowska 2001), using the plasma emission code MEKAL (Kaastra 1992; Liedahl, Osterheld, & Goldstein 1995). The main aim of this analysis was to constrain the coronal element abundances and to investigate the plasma parameters that characterize the larger flare event. Because of the limited number of events, data were combined from all times deemed to be free of significant flaring (Q1+Q2+Q3+Q4), in order to create a composite quiescent spectrum. For the flare analysis, we used events from interval F1.

Energies in the range 0.3–2.0 keV were considered; below this energy range the ACIS-S response becomes uncertain, while at higher energies the data consist largely of background events. Parameter estimation was performed using the modified χ^2 statistic (Gehrels 1986) and was verified using the C statistic (Cash 1979). Results are summarized in Table 2.

3.2. *Quiescent Spectrum*

As noted in § 1, the photospheric metallicity of α Cen AB (and by plausible extension, Proxima Cen) is known to be at least as high as the Sun's. We therefore first attempted to match the composite quiescent spectrum with isothermal models corresponding to the solar photospheric composi-

TABLE 2
Summary of Model Parameter Estimation

	Quiescent			Flare		
Model	Metallicity[a]	kT (keV)	Normalization[b]	Metallicity[a]	kT (keV)	Normalization[c]
Isothermal, solar abundance	[M/H] ≡ 0	0.31 ± 0.01	4.1 ± 0.1	...	...	...
Isothermal, abundance-free	$[M/H] = -1.0^{+0.1}_{-0.05}$	0.50 ± 0.03	2.0 ± 0.1	...	...	...
Isothermal, grouped abundance.....	[Fe/H] = −0.9 ± 0.1	0.37 ± 0.03	22 ± 2	$[Fe/H] = -0.6^{+0.5}_{-0.2}$	$0.81^{+0.4}_{-0.1}$	11^{+7}_{-4}
	[Mg/H] = −0.2 ± 0.2	0.37 ± 0.03	22 ± 2	$[Mg/H] = 0.1^{+0.4}_{-0.3}$	$0.81^{+0.4}_{-0.1}$	11^{+7}_{-4}
	[Ne/H] = −0.2 ± 0.1	0.37 ± 0.03	22 ± 2	[Ne/H] < 0.8	$0.81^{+0.4}_{-0.1}$	11^{+7}_{-4}
	[O/H] = −0.7 ± 0.1	0.37 ± 0.03	22 ± 2	...	...	...
Multithermal, solar abundance	[M/H] ≡ 0	1.37	4.6 ± 0.3	[M/H] ≡ 0	1.37	92 ± 14
		0.68	1.4 ± 0.3		0.68	16 ± 9
		0.34	1.4 ± 0.2		0.34	8.5 ± 7.2
		0.17	1.5 ± 0.4	...	...	...
		0.085	<3.9	...	...	...

[a] All abundances are expressed in the usual logarithmic bracket notation relative to solar photospheric abundances tabulated by Anders & Grevesse 1989. See also § 3.2.

[b] Normalizations for fits to the quiescent spectrum must be multiplied by 19.2 to account for the loss of events due to pile-up. The adjusted normalizations correspond to the plasma EM in units of $10^{-19}/(4\pi D^2) \int n_e n_H \, dV$, where D is the distance to Proxima Cen (1.30 pc) and n_e and n_H are the electron and hydrogen number densities, respectively.

[c] For the flare fits, normalizations must be multiplied by 21.1 to correct for pile-up losses.

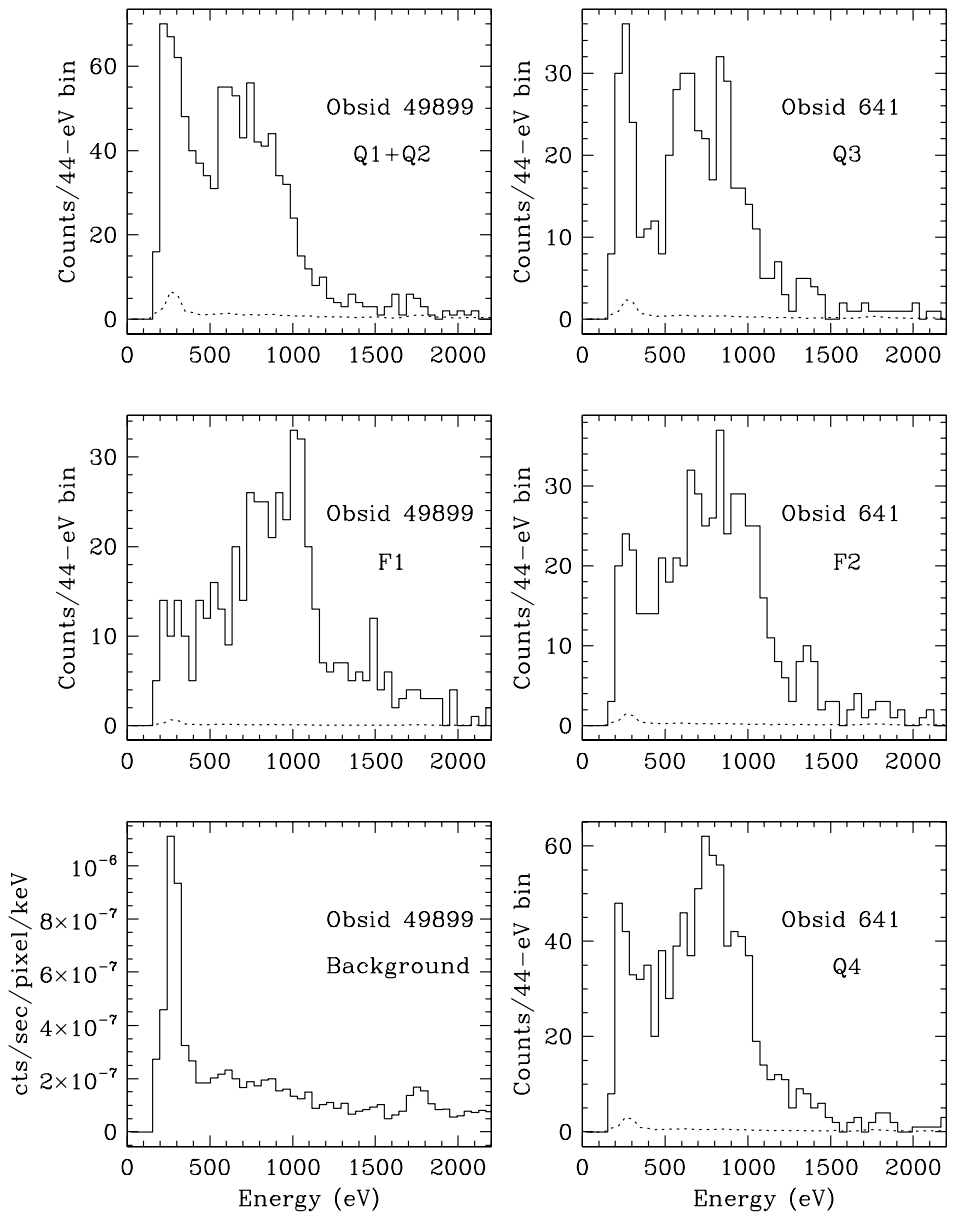

FIG. 3.—Extracted source spectra for each time segment and the background spectrum. The relative contribution of the background (*dotted curves*) varies in each source spectrum because of the different extraction areas and source rates for each time segment.

tion tabulated by Anders & Grevesse (1989). It should be noted that this abundance tabulation has been superseded by subsequent compilations of Grevesse and coworkers (see, e.g., Grevesse & Sauval 1998), although the differences are generally small ($\lesssim 0.1$ dex) for the abundant elements relevant to our study (N, O, Ne, Mg, Si, S, Ar, and Fe). Two exceptions are worthy of remark here: first, Fe, for which Grevesse & Sauval (1998) adopt recent solar photospheric results that are in agreement with the value obtained from carbonaceous chondrites, $[\mathrm{Fe/H}] = 7.50$, instead of $[\mathrm{Fe/H}] = 7.67$; second, O, for which there is a recent solar measurement based on a non-LTE analysis of forbidden O I lines indicating an abundance of $[\mathrm{O/H}] = 8.69 \pm 0.05$ (Allende Prieto, Lambert, & Asplund 2001)—0.24 dex lower than the Anders & Grevesse (1989) value. While noting these differences between currently accepted values of solar photospheric abundances and those of Anders & Grevesse (1989), we retain the latter for our model analysis partly for convenience (this compilation is "hard-wired" into the SHERPA fitting engine), but also to easily enable cross-comparison of our fitting results with those of other studies. As will be seen, it turns out that these abundance differences are in any event of little consequence for our modeling.

It was readily apparent that isothermal models were inadequate for representing the data in the vicinity of 1 keV, below 0.5 KeV, and near 0.65 KeV (Fig. 4*a*). The sense of the latter discrepancy is a model flux that is significantly higher than the data indicate; the peak in the model here is largely caused by the resonance Lyα line of H-like O.

Allowing the global metal abundance parameter to vary yielded better matches (Fig. 4*b*), although with systematic problems near 0.6 keV. The best fit, although still poor, in this case was for a metal abundance relative to the solar photosphere of $[\mathrm{M/H}] = -1.0$. The plasma temperature parameter was also significantly different from that for the solar photospheric abundance case: $0.5kT$ (5.8×10^6 K),

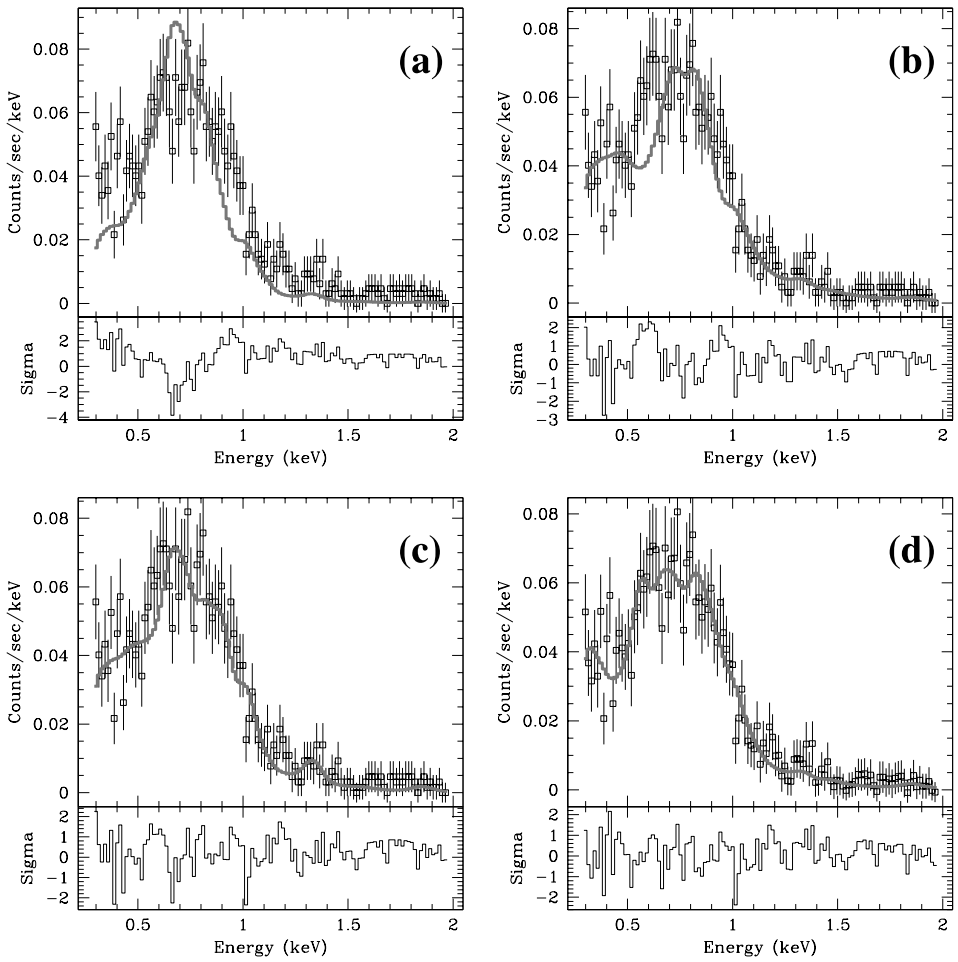

FIG. 4.—Composite quiescent spectrum, best-fit model, and residuals using the MEKAL radiative loss model with various assumptions. (*a*) Fixed solar photospheric abundances ([M/H] = 0.0). (*b*) Global metallicity scaling allowed to vary. The best-fit model corresponds to a metallicity of [M/H] = −1.0. (*c*) Grouped element abundances allowed to vary independently. The most important elements in the four groups are O, Ne, Mg, and Fe. The best-fit model has Ne and Mg abundance parameters somewhat higher than that for Fe (see text). (*d*) Multithermal model with fixed metallicity, [M/H] = 0.0. The optimum EMs of the different temperature components are illustrated in Fig. 5.

versus $0.3kT$ (3.5×10^6 K) for the latter. An improved fit (Fig. 4*c*) was obtained by varying the abundances, which we grouped together because of the limited number of counts: C, N, and O; Na, Mg, Al, Si, and S; Ne and Ar; and Fe, Ca, and Ni. The most likely temperature for this case, $0.37kT$ (4.3×10^6 K), is similar to that obtained with fixed solar abundances ($0.31kT$). Note that in this case, the abundance parameters for the Ne and Mg groups appear to be somewhat higher than those for the Fe and O groups (see Table 2); this is further discussed below.

While an isothermal model with varying element abundances matches our data within statistical uncertainties, we also investigated the propriety of multithermal models with restricted abundance parameters. We find that a model composed of four isothermal components on a regular logarithmic temperature grid ($\log T = 6.3$, 6.6, 6.9, and 7.2), all with solar photospheric abundances, also provides an acceptable match to the observations. The emission measure (EM) parameters of the different components for the optimum match are illustrated in Figure 5, together with the EMs for the different isothermal models.

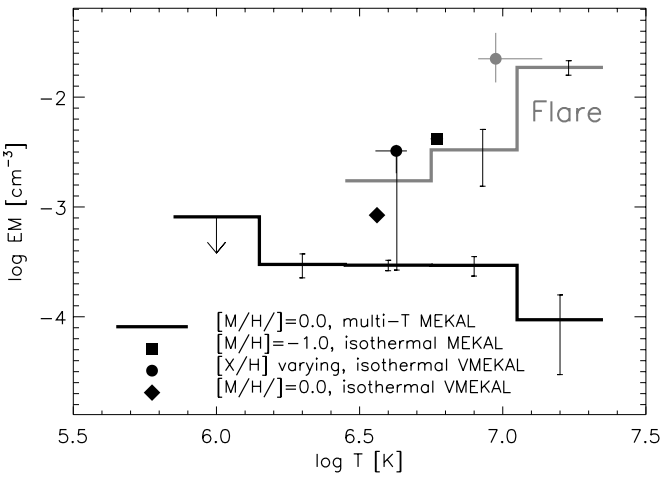

FIG. 5.—ACIS-S EM parameters for the best-fit multithermal models of flare and quiescent spectra, together with individual EMs from the various isothermal models. Error bars were estimated using the full error projection utility in the CIAO tool SHERPA.

3.3. *Flare Spectrum*

The flare interval F1 contains fewer events than the period of quiescence, so data were grouped to yield a minimum of 10 counts in a single bin. Because F1 includes data from the flare rise, peak, and much of the decay, we would not expect the spectrum to be well fitted with a single temperature. Nevertheless, an isothermal model with varying abundance parameters (grouped as for the quiescent spectral fits) is found to be acceptable within the fairly large uncertainties of the data, although an isothermal model with a solar photospheric abundance parameter is not. The acceptability of the first fit, however, is likely just a reflection of the poor statistical quality of the data, and we hesitate to draw any firm conclusions regarding abundances. One could argue, however, that if the source were indeed isothermal, then there is evidence of a higher Fe abundance during the flare than during quiescence. Again, however, a multithermal model ($\log T = 6.6$, 6.9, and 7.2) with solar photospheric abundances was found acceptable. Adding another component at $\log T = 7.5$ did not yield any significant improvement to the fit. Results for all three model fits—isothermal with solar abundances, isothermal with variable abundances, and multithermal with solar abundances—are summarized in Table 2.

3.4. *Discussion*

It is clear from the formal spectral analysis that the decimation of photon events resulting from pile-up compromises the data to an extent that useful formal constraint of model abundance parameters is not possible for either quiescent or flare emission. However, in both cases, insistence on an isothermal source model would imply that the Fe abundance is considerably lower than the solar coronal value and that Ne in particular is likely enhanced relative to Fe. Such a pattern would be in keeping with the recent results based on *Chandra* and *XMM-Newton* high-resolution spectra of the RS CVn type binaries HR 1099 (V711 Tau) and II Peg, in which strong Ne enhancements over Fe were uncovered (Brinkman et al. 2001; Drake et al. 2001; Phillips et al. 2001; Maggio et al. 2002). Moreover, Drake et al. (2001) found from a literature survey that parameter estimation analyses of low-resolution *ASCA* spectra of many other active stars tended to yield abundance parameters for Ne significantly higher than those for Fe, suggesting that the phenomenon is universal in active stars.

Unfortunately, the quiescent data are also consistent with a multithermal model with photospheric abundances. We have no observational evidence to favor one solution over another, although we do remark that the multithermal model EMs tend to appear flatter as a function of temperature than might be expected based on EMs derived for other stars (see, e.g., Fig. 2 in the review of Bowyer, Drake, & Vennes 2000). We suggest, then, that the ACIS-S spectrum presents some evidence that the coronal abundance anomalies uncovered in other active stars are also shared by our nearest neighbor.

In the case of the analysis of the flare interval F1, we are again stymied by poor data quality resulting from pile-up. Similar conclusions apply regarding the equal applicability of models in which either abundance parameters are allowed to vary or additional temperature components are added. In this regard, we note that at some level the method of parameter estimation using test statistics applied to a large spectral range becomes meaningless when there are obvious systematic differences between model and data in any much narrower spectral interval: a test statistic that indicates statistical concordance between model and data (e.g., reduced $\chi^2 < 1$) does not tell the whole story, and the propriety of the model becomes dependent on the energy range adopted for computation of the statistic. In particular, the variable-abundance parameter and multithermal models are both equally appropriate, based on the test statistic applied to the interval shown, but in the range 0.7–1 keV the multithermal model with solar photospheric abundances presents an aesthetically better representation of the data.

3.5. *Quiescent Activity Level in the Context of Earlier Observations*

Haisch et al. (1998) presented a comparison of their *RXTE* observations of Proxima Cen with earlier measurements obtained by different satellites. These disparate data were compared via isothermal EM-versus-temperature loci. These types of curves are described in detail by Drake (1999). In brief, the EM-temperature (EM-T) locus is given by the isothermal plasma EM at temperature T that yields the observed broadband count rate. The observed count rates and different responses of the various instruments that have observed Proxima Cen each define a different locus in the EM-T plane. Since, in the case of stellar coronae, the plasma is not likely to be isothermal, the individual loci actually represent the upper limit to the plasma EM at any given T. If the true EM distribution is relatively sharply peaked and the bandpasses in question are largely dominated by lines formed at this peak temperature, then the isothermal approximation can be reasonable.

We have taken the EM-T loci for the different instrument count rates reported for Proxima Cen from Haisch et al. (1998) and show these in Figure 6. One small difference between our Figure 6 and Figure 3 of Haisch et al. (1998)

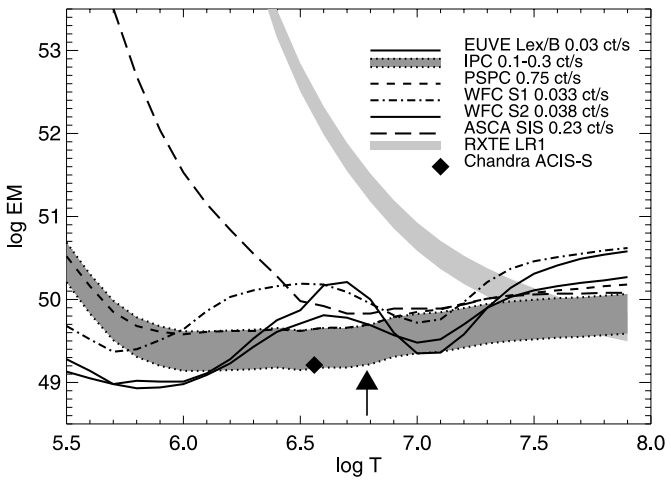

FIG. 6.—Loci of isothermal EM vs. isothermal plasma temperatures that correspond to different instrument count rates reported for Proxima Cen in the literature for observations between 1979 and 1996. The diamond corresponds to the isothermal EM and temperature found in the optically thin, collision-dominated model parameter estimation analysis for the case of solar photospheric abundances. Here the units of EM have been converted to the logarithm of the product $N_e^2(T)V(T)$ in units of cm^{-3}. The arrow indicates the isothermal plasma temperature obtained by Haisch, Antunes, & Schmitt 1995 from their *ASCA* observation.

concerns the *Einstein* locus, which we represent here (*shaded region*) as including the range of apparently quiescent count rates 0.1–0.3 counts s^{-1} from the 1979 March 6–7 and 1980 August 20 observations (Haisch et al. 1980, 1983). The point corresponding to our *Chandra* ACIS-S EM for an isothermal model for solar photospheric abundances overlaps with this *Einstein* locus, but lies at the lower end of the range of EMs previously obtained in the temperature range $\log T = 6.5$–6.8 that characterizes the quiescent coronal temperatures found for Proxima Cen. We have used the solar photospheric abundance point because the other loci are also based on a radiative loss model with solar photospheric abundances; the EMs obtained when the global metallicity and grouped element abundances were allowed to vary in the parameter estimation process are higher by about 0.6 and 0.7 dex, respectively, and shift to slightly higher temperatures. The isothermal plasma temperature we obtain from our model parameter estimation for solar photospheric abundances, 0.31 keV (3.6×10^6 K; $\log T = 6.56$), is slightly cooler than the 6.1×10^6 K obtained from the *ASCA* observation by Haisch et al. (1995; *arrow*), but it is very similar to the estimates of 4×10^6 K by Haisch et al. (1980, 1983) based on the *Einstein* observations. Proxima Cen thus appears to have been in a relatively low state of activity at the time of the *Chandra* observation.

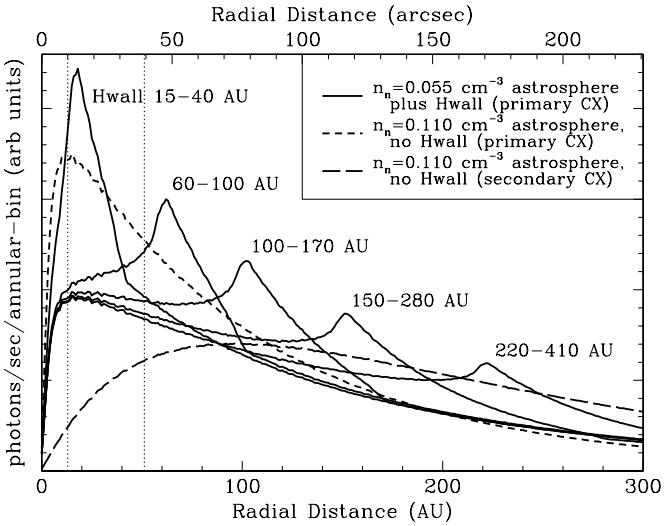

FIG. 7.—Numerical simulations of CX emission distribution around Proxima Cen. Solid lines are for models with a hemispherical hydrogen wall with twice the ISM neutral density at various distances from the star and half the ISM density inside the astrosphere (behind the wall). The short-dashed curve is for when there is no hydrogen wall and the astrospheric neutral density is the same as that of the undisturbed ISM. The long-dashed curve is for the same case, but showing secondary CX emission. Vertical dotted lines mark our annular search range (13–51 AU), which contains 16%–28% of the primary CX emission and roughly one-third as much secondary emission. [*See the electronic edition of the Journal for a color version of this figure.*]

4. CX AND THE STELLAR WIND

4.1. *Spatial Distribution*

A quantitative assessment of *Chandra*'s ability to detect stellar winds and a model of the spatial distribution of astrospheric CX emission for a spherically symmetric wind have been described by Wargelin & Drake (2001). For this work, we have used a more detailed model of the interaction of Proxima Cen's stellar wind and its local ISM. As noted in § 1, a "hydrogen wall" of neutral gas is expected to form when an ionized wind interacts with neutral gas in the ISM, with a strong density enhancement on the "upwind" side when the star and surrounding gas have relative motion.

Proxima Cen and α Cen are surrounded by the "G cloud," for which Linsky et al. (2000) have derived a value of 0.10 cm^{-3} for the neutral H density, $n_{\rm H\ I}$, based on absorption-line spectra obtained by *HST* and *EUVE*. The G cloud is moving roughly toward us from the direction of Proxima Cen, toward $l = 184.^\circ5$, $b = -20.^\circ5$ (Lallement & Bertin 1992), with virtually the same velocity and direction of motion as the Local Interstellar Cloud surrounding the Sun. Wood et al. (2001; see their Fig. 3) modeled the wind-cloud interaction for a range of mass-loss rates and showed that the neutral gas density within the hydrogen wall was approximately twice that in the undisturbed ISM, while behind the wall, inside the astrosphere, the neutral density was about half that in the undisturbed gas.

Because of Proxima Cen's position and the cloud's direction of motion, the distribution of gas around it should be approximately symmetric from our viewpoint. We use a simplified model of the Wood et al. results, taking $n_{\rm H\ I} = 0.10$ cm^{-3} in the undisturbed ISM, 0.20 cm^{-3} in a hemispherical shell on the upwind side, and 0.05 cm^{-3} inside and behind the shell, in the astrosphere. Several hemisphere sizes were considered, as shown in Figure 7, corresponding to mass-loss rates of 2, 1, 0.5, 0.2, and $\sim$0.05 $\dot{M}_\odot$ (the last case being our own extrapolation). Near the star, $n_{\rm H\ I}$ is lower than the asymptotic astrospheric value because of CX with the densest part of the solar wind (mostly protons), as well as radiation pressure and photoionization. We use the simple Cravens (2000) model for neutral gas density within the astrosphere, $n_n(r) = n_{n0}e^{-\lambda_n/r}$, where n_{n0} is the neutral gas density far from the star (0.05 cm^{-3}) and λ_n is the scale for neutral gas depletion. For the Sun, λ_n for hydrogen is roughly 5 AU upstream and 20 AU downstream. Because Proxima Cen's mass-loss rate $\dot{M}$ is comparable to or less than the Sun's and λ_n scales as roughly $\dot{M}^{0.5}$, we assume that $\lambda_n = 5$ AU; the actual value is of little importance to our results.

As seen in Figure 7, when projected on the sky and summed in annular bins around the star, the CX emission profile rises steeply from the center and then slowly falls. The deficit of emission at small radii is because of the aforementioned neutral gas depletion near the star. Local maxima at intermediate radii arise from sight lines through the sides of the hemispherical hydrogen wall, where CX emission is enhanced because of the higher neutral density. The general falloff in X-ray CX emission at large radii occurs because highly charged ions are "used up" as they change-exchange with neutral gas, recombining into lower charge states that cannot emit at X-ray energies. We refer to CX emission from ions in their initial (coronal) charge state as "primary" emission (i.e., bare→H-like or H-like→He-like CX), while photons from the second step of bare→H-like→He-like CX are "secondary" emission.

The path length for CX is equal to $1/n_n\sigma_{\rm CX}$, where n_n is the total neutral gas density and $\sigma_{\rm CX}$ is the cross section for CX. The He/H abundance ratio is $\sim$10%, and He should have at least as high a fraction of neutral atoms as H because of its higher ionization potential, so we conserva-

tively set $n_n = 1.1 n_{\rm H\,I}$. Few experimental measurements of CX cross sections are available, and theoretical calculations have large uncertainties, but a good compilation of available data on C and O ions colliding with H, He, and H_2 is that of Phaneuf, Janev, & Pindzola (1987). Cross sections for C, N, and O, along with estimated uncertainties and the dominant CX capture energy levels, are listed in Table 3, assuming a wind velocity of 550 km s^{-1}. For comparison, the slow solar wind has a velocity of roughly 400 km s^{-1} (800 km s^{-1} for the fast wind), but Proxima Cen's wind is probably somewhat faster, given its higher coronal temperature. (The significance of slow vs. fast winds is discussed in § 4.2.) The actual velocity is not very important, as the relevant CX cross sections vary by no more than about ±10% between 400 and 700 km s^{-1}.

To obtain an average $\sigma_{\rm CX}$ for use in our spatial emission simulations, we applied a 10:1 weighting for H:He cross sections, with further weighting for each ion species according to its emission contribution in the energy range of interest (see § 4.2). We thus obtain an average cross section of 4.6×10^{-15} cm^2. With $n_n = 0.055$ cm^{-3} inside the astrosphere, the path length for CX around Proxima Cen is then ~240 AU (60 AU in the hydrogen wall and 120 AU in the undisturbed ISM).

Proxima Cen's CX emission is thousands of times weaker than its coronal emission, so the best place to look for CX photons is in the wings of the PSF, but not so far out that the background per unit radius (in annuli around the star), which increases linearly with radius, becomes too large. For Proxima Cen, our analysis shows that a good choice is an annulus with inner and outer radii of 20 and 80 pixels, corresponding to 10″ and 39″, or 13 and 51 AU. The fraction of primary CX emission, $f_{\rm CX1}$, within this annulus lies between 0.16 and 0.28, depending upon the hydrogen wall location (higher fractions for smaller H walls). Those same limits apply to the cases in which the H wall is at infinity or does not exist at all (so the astrospheric neutral density is the same as in the undisturbed medium), respectively. We therefore adopt $f_{\rm CX1} = 0.22$ as the most likely value. The fraction for secondary CX, $f_{\rm CX2}$, is about 30% as large as $f_{\rm CX1}$.

TABLE 3
CHARGE EXCHANGE CROSS SECTIONS

Ion	Neutral Species	$\sigma_{\rm CX}$ (10^{-15} cm^2)	Uncertainty (%)	Capture Levels
C^{5+}	H	2.2[a]	20	$n = 4$
	He	1.5[a]	50	$n = 3$
C^{6+}	H	3.9[a]	20	4*f*, 4*d*
	He	0.9[a]	40	3*p*, 3*d*
N^{7+}	H	5.0[b]	30	$n = 5$
	He	3.0[c]	40	$n = 4$
O^{7+}	H	5.1[a]	20	$n = 4, 5$
	He	1.5[a]	30	$n = 4$
O^{8+}	H	5.0[a]	20	5*f*, 5*g*, 5*d*
	He	3.0[a]	30	$n = 4$

[a] Data from Phaneuf et al. 1987, assuming a collision velocity of 550 km s^{-1}. Cross sections vary by less than 10% from the listed value between 400 and at least 700 km s^{-1}.

[b] The theoretical cross sections of Harel, Jouin, & Pons 1998 for O^{8+} and N^{7+}+H are virtually identical (5.66×10^{-15} cm^2 at 440 km s^{-1}), so we apply the Phaneuf et al. 1987 value for O^{8+} to N^{7+}.

[c] By analogy, we use the same cross section for N^{7+}+He as for O^{8+}+He. Cross sections for He-like Si, He-like and Li-like S, and H-like N^{6+} are assumed to be 4×10^{-15} cm^2; these are minor contributors, and errors in their cross sections are unimportant.

In addition to studying the effect of the hydrogen wall, we also examined the sensitivities of $f_{\rm CX1}$ and $f_{\rm CX2}$ to variations in the values of λ_n and $n_n \sigma_{\rm CX}$. Varying λ_n by a factor of 3, corresponding to roughly a factor of 10 in mass-loss rate, had little effect (less than 15% for $f_{\rm CX1}$). The overall uncertainty in $\sigma_{\rm CX}$, keeping in mind the dominance of O CX, is 20%–30%. Linsky et al. (2000) do not list a formal uncertainty on $n_{\rm H\,I}$ for the G cloud, but it appears to be comparable or smaller. A 50% error in $n_n \sigma_{\rm CX}$, which is therefore rather pessimistic, leads to roughly a 40% change in $f_{\rm CX1}$ (33% higher $f_{\rm CX1}$ with larger $n_n \sigma_{\rm CX}$, 42% lower with smaller $n_n \sigma_{\rm CX}$). Variation in $f_{\rm CX2}$ is somewhat larger, but it is less important because of its smaller contribution to total emission within the chosen annulus. Including uncertainties such as those in the various hydrogen wall parameters and simplistic spatial models yields an overall uncertainty of roughly a factor of 2 in the value of $f_{\rm CX}$.

4.2. *Spectrum*

To further increase the contrast of CX emission against coronal X-rays and the background, we focus on a narrow energy range around He-like O Kα for several reasons: oxygen is the most abundant metal species in stellar winds; a large fraction of oxygen ions in Proxima Cen's wind are highly charged (bare and H-like) and therefore emit CX X-rays; nearly all the CX X-ray emission from He-like ions is emitted as Kα photons ($n = 2 \rightarrow 1$ transitions; 561–574 eV), because selection rules inhibit direct radiative decay to ground from higher n levels; coronal emission is relatively brighter at higher energies; and the ACIS detection efficiency decreases rapidly at lower energies, while the background rises steeply (see Fig. 3, *bottom left panel*).

To decide how wide to make the energy range, and to determine the expected photon detection rate, we constructed a simple model of the expected CX spectrum, including emission from C and N as well as from O. Other ions either have insignificant abundances or do not emit X-rays near 570 eV (with the minor exceptions of Li-like Si and S, which we discuss later). As noted above, H-like ions charge-exchange to create He-like ions, which emit Kα photons almost exclusively. Bare ions charge-exchange into H-like ions, preferentially populating the $n \sim q^{0.7}$ level (see Table 3), where q is the ion charge. Modeling the resulting cascade process is difficult and depends on, among other things, knowing the initial sublevel population distribution immediately following electron transfer, but roughly half of the excited electrons will decay directly to ground and the other half will cascade down to the $n = 2$ level and then emit a Lyα photon (Kharchenko & Dalgarno 2001; Beiersdorfer et al. 2000). The ACIS-S FWHM energy resolution is ~130 eV at the energies of interest here, compared to the tens of eV separating high-n levels in H-like C, N, and O, so the exact distribution of high-n Lyman series emission is unimportant in our analysis. Model line energies and *Chandra*'s effective area at each energy are listed in Table 4.

We assume that elemental abundances in Proxima Cen's wind are the same as for the Sun, and we model its ionic composition by analogy to the "slow" solar wind, with adjustments to reflect the higher temperature of Proxima Cen's corona. The solar abundances, ion fractions, and "freezing-in" temperatures ($T_{\rm freeze}$) listed in Table 5 are

TABLE 4
MODELED CX EMISSION LINES

Line	Energy (eV)	Effective Area (cm^2)
C Kα.....	304	55
C Lyα	368	200
C Lyγ.....	459	322
N Kα	426	274
N Lyα	500	371
N Lyγ	625	416
O Kα.....	570	359
O Lyα	654	443
O Lyδ.....	836	561

NOTE.—H-like Lyman emission is assumed to be divided equally between Lyα and transitions from the CX capture level directly to ground. Effective areas have an uncertainty of approximately 10%.

taken from the tabulations of von Steiger et al. (2000) and Schwadron & Cravens (2000), based on data collected by the *Ulysses* Solar Wind Ion Composition Spectrometer at a distance of roughly 1 AU from the Sun. Note that the $T_{\rm freeze}$-values, which characterize the ionization state of elements within the wind, are much higher than the kinetic temperature of the wind, which is only of order 10^4 K.

The justification for basing our model on solar slow-wind parameters has two parts. The first is the much greater surface coverage of active areas on Proxima Cen, compared to the Sun. On the Sun, it is these active regions that are the source of the slow wind. The observed coronal X-ray flux from Proxima Cen in quiescence, after correction for pile-up, is about 3×10^{-12} ergs cm^2 s^{-1}, corresponding to a total coronal luminosity of somewhat more than 1×10^{27} ergs s^{-1} (including a factor of 2 to account for the unseen side of the stellar disk). This level is comparable to the typical value for the total solar coronal X-ray luminosity at solar maximum, derived by Peres et al. (2000), of 4.7×10^{27} ergs s^{-1}. Based on the radius of 0.17 $R_\odot$ for Proxima Cen (Reid & Gilmore 1984), the surface X-ray flux of Proxima Cen during the *Chandra* observation is a factor of $\sim$10 higher than that of the Sun during solar maximum. If the coronal plasma density of Proxima Cen is comparable to that of solar active regions, as seems likely based on *Chandra* measurements for other active M dwarfs (see, e.g., Güdel et al. 2001; Maggio et al. 2002), then the surface coverage of emitting regions on Proxima Cen is significantly greater than that on the Sun during its most active time. Indeed, Lim et al. (1996b) deduced from radio observations that up to 88% of Proxima Cen's surface might be covered by nonflaring active regions and that up to 13% might be covered by even hotter flaring regions. Our second argument is that any "fast" wind, although it will be somewhat less ionized than the slow wind ($\Delta \log T_{\rm freeze} = -0.16$ for C and O in the solar wind), will still be "hot" enough that nearly all C and N and most O ions will be either fully ionized or H-like.

TABLE 5
PARAMETERS FOR THE SLOW SOLAR WIND

Element	Relative Abundance	H-like Fraction	Bare Fraction	log $T_{\rm freeze}$ (K)
C.....	0.670	0.31	0.48	6.13
N	0.0785	0.74	0.08	6.15
O.....	1	0.20	0.07	6.20

NOTE.—Data are taken from von Steiger et al. 2000 and Schwadron & Cravens 2000. The value of $T_{\rm freeze}$ for N ions was not listed, and it is our estimate. As noted by von Steiger et al., a single-temperature characterization becomes problematic with increasing Z; based on the tabulation of Mazzotta et al. 1998, we estimate that the best log $T_{\rm freeze}$ value for O lies between 6.2 and 6.3. For the fast solar wind, log $T_{\rm freeze}$ is roughly 0.16 lower for each element.

To estimate the fraction of bare and H-like C, N, and O ions in Proxima Cen's wind, we use the ion balance tabulations of Mazzotta et al. (1998), with freezing-in temperatures based on solar values, but scaled up to reflect Proxima Cen's hotter corona. At solar maximum, log $T_{\rm corona} = 6.30$, while for Proxima Cen, log $T_{\rm corona} \sim 6.55$, excluding its frequent flares, which are even hotter. We therefore expect $T_{\rm freeze}$-values for Proxima Cen's wind to be at least $\Delta \log T = 0.25$ higher than for the solar wind. As shown in Table 5, von Steiger et al. (2000) state that log $T_{\rm freeze} = 6.20$ for O in the slow solar wind, but they note that a single-temperature characterization becomes increasingly suspect for higher Z elements. Based upon the actual ion fractions listed by Schwadron & Cravens (2000) and comparisons to the Mazzotta et al. (1998) tables, we find that log $T_{\rm freeze} = 6.20$ best matches the H-like O ion fraction, while log $T_{\rm freeze} = 6.30$ corresponds to the observed bare O fraction. We therefore assume that the best value of log $T_{\rm freeze}$ for O ions in Proxima Cen's wind is $6.25 + 0.25 = 6.50$ and for C and N roughly 6.40 (see Table 5). The exact value for C and N is unimportant, because C is more than 90% fully ionized above log $T = 6.30$ and N contributes only a few percent to the total emission within the energy range of interest.

To allow for uncertainty in the actual ion fractions, we created model spectra for log $T_{\rm freeze} = 6.4$, 6.5, and 6.6. The intensity of each line was weighted by elemental abundance relative to O, ion fraction, line yield (1 for He-like Kα and 0.5 for Lyα and the high-n Lyman lines), fraction of emission within the chosen annulus ($f_{\rm CX1}$ or $f_{\rm CX2}$, as appropriate), and *Chandra*/ACIS-S effective area at the line energy. Results, assuming a detector energy resolution of 130 eV, are shown in Figure 8.

Based on those spectra, and with the aim of maximizing the contrast of CX emission versus the corona and the detector background, we chose the energy range 453–701 eV. This range contains 97% of the ACIS pulse-height distribution for the O Kα line, 80% of O Lyα, and 54% of C Lyγ. After we assigned these last weighting factors to each line, the net effective area for detecting CX photons, normalized to O abundance ($A_{\rm relO}$ in cm^2), was then calculated for each of the three models. The results, using freezing-in temperatures of log $T = 6.4$, 6.5, and 6.6, are $A_{\rm relO} = 73$, 82, and 83 cm^2, respectively. The fraction of bare or H-like O ions ranges from 77% to 97%, and oxygen emission contributes very nearly 76% of the total $A_{\rm relO}$ in each case. For comparison, $A_{\rm relO} = 28$ cm^2 for the slow solar wind, and $A_{\rm relO} = 137$ cm^2 if all ions are fully stripped.

He-like Si ions have significant abundance at the $T_{\rm freeze}$-values we assume and emit Li-like 5, $6 \rightarrow 3$ CX photons around 460 eV. Li-like and Be-like S also contribute some emission, adding another $\sim$6 cm^2 to $A_{\rm relO}$, assuming $\sigma_{\rm CX} \sim 4 \times 10^{-15}$ cm^2. We adopt a total $A_{\rm relO} = 85$ cm^2, with

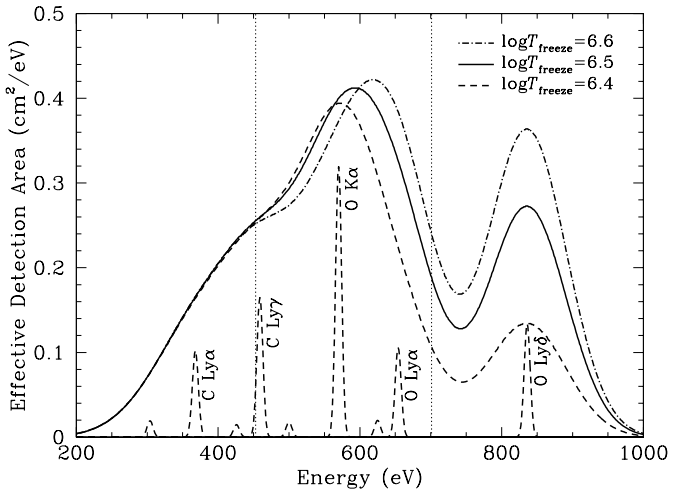

FIG. 8.—Model spectra of CX emission from Proxima Cen's wind within an annulus of radii 10″ and 39″, with ACIS resolution of 130 eV FWHM. Ion balances were derived from Mazzotta et al. 1998 for three freezing-in temperatures, assuming slow solar wind element abundances (von Steiger et al. 2000). The integrated area under each curve and between the dotted vertical lines (marking the energy range of interest) is equal to the effective area for detection of photons within that energy range and annulus by *Chandra*. Major emission lines at $\log T_{\rm freeze} = 6.4$ are also shown, with 10 eV resolution. The minor contributions of Si and S ions are not included. [*See the electronic edition of the Journal for a color version of this figure.*]

an uncertainty of 10–15 cm^2 to reflect the spread among results from the different ionization models and to allow for uncertainties in the applicability of the slow-wind scenario. We allow another 10–15 cm^2 for uncertainties in radiative branching ratios (primarily for the Lyman lines). Errors caused by uncertainties in the abundances of C, N, Si, and S will be small, because O dominates the spectrum. Adding the errors in quadrature, we estimate that the net uncertainty in $A_{\rm relO}$, exclusive of errors in $f_{\rm CX1}$ and $f_{\rm CX2}$, which were already discussed, is no more than 25 cm^2.

4.3. *Determination of Mass-Loss Limit by Comparison of Quiescent and Flare PSFs*

Very accurate knowledge of *Chandra*'s PSF in the specific energy range of interest (453–701 eV) is required in order to look for an excess arising from CX emission. Rather than relying on existing PSF models, which are well calibrated at only a few widely spaced energies and even then appear to underestimate the amount of power in the wings, we use the *observed* PSF during the bright flare (F1), which will have negligible contamination by any CX emission. The PSF is roughly independent of photon energy below ~1 keV, so we use a slightly larger energy range (307–1007 eV) for the flare to improve the statistics. The fraction of flare events in the chosen energy range contained within the annulus of radii 10″ and 39″ is then compared against the fraction in the same annulus during the time when the coronal emission is weakest (Q1+Q2) and CX photons will be easiest to see.

We find that the fractions are the same to within statistical uncertainty. Based upon the fraction of flare events (0.0096 ± 0.0019), 57 ± 12 events would be expected during the quiescent period in the absence of any CX counts, while 39 ± 11 were observed. We can, however, put an upper limit on the mass-loss rate by computing how many events beyond the expected 57 would be required to detect a statistically significant CX signature. We find that 17 excess events would be required for a 1 σ detection, 36 for 2 σ, and 61 for 3 σ.

We convert those detection limits to mass-loss rates by comparing the number of CX counts expected if Proxima Cen's wind has the same element abundances as the solar wind. The number of detected events is given by

$$N_{\rm det} = \frac{R_{\rm O} A_{\rm relO} t}{4\pi d^2} , \qquad (1)$$

where $R_{\rm O}$ is the rate at which O ions are injected into the wind, $A_{\rm relO}$ is the net effective area (normalized to O abundance), taking into account all the spatial and spectral detection details described in §§ 4.1 and 4.2, t is the exposure time, and d is the distance to Proxima Cen (1.30 pc).

The solar mass-loss rate, $\dot{M}_\odot$, is $2 \times 10^{-14}\ M_\odot\ {\rm yr}^{-1}$, where $M_\odot$ is 2×10^{33} g. With abundance ratios of 0.044 for He relative to H (Schwadron & Cravens 2000) and 0.002 for heavier elements, the average wind ion has a mass of 1.155 amu, which yields a total rate of 6.57×10^{35} ions s^{-1} injected into the wind, of which 6.27×10^{35} ions s^{-1} are hydrogen. Schwadron & Cravens list the O abundance relative to H as 5.6×10^{-4}, so $R_{\rm O} = 3.51 \times 10^{32}$ O ions s^{-1}. The total Q1+Q2 exposure time t is 28,688 s, and $A_{\rm relO} = 85$ cm^2, so $N_{\rm det} = 4.2$ counts are expected for a 1 $\dot{M}_\odot$ mass-loss rate. Comparing this with the statistical upper limits on observed counts derived earlier, we see that the 1 σ upper limit on Proxima Cen's mass-loss rate is 4.0 $\dot{M}_\odot$, with 8.6 $\dot{M}_\odot$ and 14 $\dot{M}_\odot$ for the 2 σ and 3 σ limits, respectively.

As discussed at the end of § 4.1, systematic uncertainties in our model of the spatial distribution of CX emission lead to roughly a factor of 2 uncertainty in our results. Errors in spectral modeling are considerably smaller, so the last major source of uncertainty is the abundance of O relative to H in the wind. We assumed that this last parameter is the same as for the Sun, but it could easily differ by 50%. Our estimate of overall model uncertainty is therefore roughly a factor of 3.

Both the systematic and statistical uncertainties should be easy to improve in the near future. The question of Proxima Cen's coronal, and therefore wind, metallicity should be answered by high-resolution spectra recently obtained by *Chandra* and *XMM-Newton*. Experimental and theoretical studies of CX cross sections and the relevant radiative pathways should likewise permit more precise spectral models in the next few years, further reducing systematic uncertainties. As for statistical limitations, ongoing improvements in the calibration of *Chandra*'s PSF in the wings will allow the derivation of tighter limits on the mass-loss rate, as would, of course, more *Chandra* observations.

Note added in manuscript.—Mass-loss rates for an additional four stars have recently been measured using the Lyα technique, as reported by Wood et al. (2002).

We gratefully acknowledge very helpful discussions with John Raymond and Vasili Kharchenko. The authors were supported by NASA contract NAS8-39073 to the *Chandra* X-Ray Center during the course of this research. B. W. was also supported by NASA's Space Astrophysics and Analysis program under grant NAG5-10443.

REFERENCES

Agrawal, P. C., Rao, A. R., & Sreekantan, B. V. 1986, MNRAS, 219, 225
Allende Prieto, C., Lambert, D. L., & Asplund, M. 2001, ApJ, 556, L63
Anders, E., & Grevesse, N. 1989, Geochim. Cosmochim. Acta, 53, 197
Anosova, J., Orlov, V. V., & Pavlova, N. A. 1994, A&A, 292, 115
Badalyan, O. G., & Livshits, M. A. 1992, Soviet Astron., 36, 70
Beiersdorfer, P., et al. 2000, Phys. Rev. Lett., 85, 5090
Benedict, G. F., et al. 1998, AJ, 116, 429
———. 1999, AJ, 118, 1086
Bond, H. E., Mullan, D. J., O'Brien, M. S., & Sion, E. M. 2001, ApJ, 560, 919
Bowyer, S., Drake, J. J., & Vennes, S. 2000, ARA&A, 38, 231
Brinkman, A. C., et al. 2001, A&A, 365, L324
Cash, W. 1979, ApJ, 228, 939
Cox, D. P. 1998, in The Local Bubble and Beyond, ed. D. Breitschwerdt, M. J. Freyberg, & J. Trümper (Berlin: Springer), 121
Cravens, T. E. 1997, Geophys. Res. Lett., 24, 105
———. 2000, ApJ, 532, L153
Cravens, T. E., Robertson, I. P., & Snowden, S. L. 2001, J. Geophys. Res., 106, 24883
Doyle, J. G., & Mathioudakis, M. 1991, A&A, 241, L41
Drake, J. J. 1999, ApJS, 122, 269
———. 2002, in ASP Conf. Ser. 277, Stellar Coronae in the *Chandra* and *XMM-Newton* Era, ed. F. Favata & J. J. Drake (San Francisco: ASP), in press
Drake, J. J., Brickhouse, N. S., Kashyap, V., Laming, J. M., Huenemoerder, D. P., Smith, R., & Wargelin, B. J. 2001, ApJ, 548, L81
Feldman, U., & Laming, J. M. 2000, Phys. Scr., 61, 222
Fleming, T. A., Giampapa, M. S., Schmitt, J. H. M. M., & Bookbinder, J. A. 1993, ApJ, 410, 387
Freeman, P., Doe, S., & Siemiginowska, A. 2001, Proc. SPIE, 4477, 76
Gayley, K. G., Zank, G. P., Pauls, H. L., Frisch, P. C., & Welty, D. E. 1997, ApJ, 487, 259
Gehrels, N. 1986, ApJ, 303, 336
Greenwood, J. B., Williams, I. D., Smith, S. J., & Chutjian, A. 2000, ApJ, 533, L175
Grevesse, N., & Sauval, A. J. 1998, Space Sci. Rev., 85, 161
Güdel, M., Audard, M., Magee, H., Franciosini, E., Grosso, N., Cordova, F. A., Pallavicini, R., & Mewe, R. 2001, A&A, 365, L344
Haisch, B., Antunes, A., & Schmitt, J. H. M. M. 1995, Science, 268, 1327
Haisch, B., Kashyap, V., Drake, J. J., & Freeman, P. 1998, A&A, 335, L101
Haisch, B. M., Linsky, J. L., Bornmann, P. L., Stencel, R. E., Antiochos, S. K., Golub, L., & Vaiana, G. S. 1983, ApJ, 267, 280
Haisch, B. M., Linsky, J. L., Harnden, F. R., Jr., Rosner, R., Seward, F. D., & Vaiana, G. S. 1980, ApJ, 242, L99
Harel, C., Jouin, J., & Pons, B. 1998, At. Data Nucl. Data Tables, 68, 279
Houdebine, E. R., Foing, B. H., & Rodonò, M. 1990, A&A, 238, 249
Izmodenov, V. V., Lallement, R., & Malama, Y. G. 1999, A&A, 342, L13
Jay, J. E., Guinan, E. F., Morgan, N. D., Messina, S., & Jassour, D. 1996, BAAS, 189, 120.04
Kaastra, J. S. 1992, An X-Ray Spectral Code for Optically Thin Plasmas (updated version 2.0; Leiden: Internal SRON-Leiden Report)
Kharchenko, V., & Dalgarno, A. 2001, ApJ, 554, L99
Kundu, M. R., & Shevgaonkar, R. K. 1988, ApJ, 334, 1001
Lallement, R., & Bertin, P. 1992, A&A, 266, 479
Liedahl, D. A., Osterheld, A. L., & Goldstein, W. H. 1995, ApJ, 438, L115
Lim, J., & White, S. M. 1996, ApJ, 462, L91
Lim, J., White, S. M., & Cully, S. L. 1996a, ApJ, 461, 1009
Lim, J., White, S. M., & Slee, O. B. 1996b, ApJ, 460, 976
Linsky, J. L., Redfield, S., Wood, B. E., & Piskunov, N. 2000, ApJ, 528, 756
Maggio, A., Drake, J. J., Kashyap, V., Peres, G., & Sciortino, S. 2002, in ASP Conf. Ser. 277, Stellar Coronae in the *Chandra* and *XMM-Newton* Era, ed. F. Favata & J. J. Drake (San Francisco: ASP), in press
Matthews, R., & Gilmore, G. 1993, MNRAS, 261, L5
Mazzotta, P., Mazzitelli, G., Colafrancesco, S., & Vittorio, N. 1998, A&AS, 133, 403
Mullan, D. J., Doyle, J. G., Redman, R. O., & Mathioudakis, M. 1992, ApJ, 397, 225
Mullan, D. J., Sion, E. M., Bruhweiler, F. C., & Carpenter, K. G. 1989, ApJ, 339, L33
Müller, H.-R., Zank, G. P., & Wood, B. E. 2001, ApJ, 551, 495
Peres, G., Orlando, S., Reale, F., Rosner, R., & Hudson, H. 2000, ApJ, 528, 537
Phaneuf, R. A., Janev, R. K., & Pindzola, M. S. 1987, Atomic Data for Fusion, Vol. 5: Collisions of Carbon and Oxygen Ions with Electrons, H, H_2, and He (ORNL-6090; Oak Ridge: Oak Ridge Natl. Lab.)
Phillips, K. J. H., Mathioudakis, M., Huenemoerder, D. P., Williams, D. R., Phillips, M. E., & Keenan, F. P. 2001, MNRAS, 325, 1500
Reid, N., & Gilmore, G. 1984, MNRAS, 206, 19
Schwadron, N. A., & Cravens, T. E. 2000, ApJ, 544, 558
Snowden, S. L., et al. 1995, ApJ, 454, 643
van den Oord, G. H. J., & Doyle, J. G. 1997, A&A, 319, 578
Vidal-Madjar, A., & Ferlet, R. 2002, ApJ, 571, L169
von Steiger, R., et al. 2000, J. Geophys. Res., 105, 27217
Wargelin, B. J., & Drake, J. J. 2001, ApJ, 546, L57
White, N. E. 1996, in ASP Conf. Ser. 109, Cool Stars, Stellar Systems and the Sun, ed. R. Pallavicini & A. Dupree (San Francisco: ASP), 193
Wood, B. E., Alexander, W. R., & Linsky, J. L. 1996, ApJ, 470, 1157
Wood, B. E., Linsky, J. L., Müller, H.-R., & Zank, G. P. 2001, ApJ, 547, L49
Wood, B. E., Müller, H.-R., Zank, G. P., & Linsky, J. L. 2002, ApJ, 574, 412